

# Design and Test of the Ground-Based L-Band Radiometer for Estimating Water in Soils (LEWIS)

François Lemaître, Jean-Claude Poussière, Yann H. Kerr, *Senior Member, IEEE*, Michel Déjus, Roger Durbe, Patricia de Rosnay, and Jean-Christophe Calvet

**Abstract**—In the framework of the preparation of the Soil Moisture and Ocean Salinity (SMOS) mission, several field experiments are required so as to address specific modeling issues. The goal is to improve current models and to test retrieval algorithms. However, adequate ground instrumentation is scarce and not readily available “off the shelf.” In this context, a high-accuracy L-band radiometer was required for a specific long-term campaign for the preparation of the SMOS mission. For this purpose, a dual-polarized radiometer was designed and built to check algorithms for surface soil moisture retrieval from multiangular dual-polarized brightness temperatures. This radiometer has been tested in the field for 20 months and is operational since end of January 2003. The aim of this paper is to give details of the system architecture, calibration procedures, together with the performances obtained and some preliminary results.

**Index Terms**—Calibration, L-band radiometry, L-Band Radiometer for Estimating Water in Soils (LEWIS), Soil Moisture and Ocean Salinity (SMOS), soil moisture.

## I. INTRODUCTION

IT IS NOW well admitted that soil moisture and sea surface salinity are required to improve meteorological and climatic predictions [1]–[4]. However, these two quantities are not yet available globally and not with an adequate temporal sampling [5]. Given continuing developments in technology, microwave radiometry is the most promising way to fill this data gap [6], [7]. It is within this framework that the European space agency (ESA) selected the second Earth Explorer Opportunity Mission, namely the Soil Moisture and Ocean Salinity (SMOS) mission. SMOS is currently being studied in the development and implementation phase (Phase-C/D) and is scheduled for launch in February 2007 [8], [9]. SMOS will exploit an innovative interferometric approach [10]–[12] with an instrument designed as a two-dimensional interferometer capable of acquiring polarized and angular brightness temperature observations at L-band (1.4 GHz) globally and with a revisit time smaller than

three days to retrieve soil moisture and ocean salinity. Both are key variables used in weather, climate, and extreme-event forecasting.

SMOS is, thus, a demonstrator with broad and ambitious scientific objectives, as the lack of global observations of salinity and soil moisture is retarding progress in many research fields. The need for these data has been highlighted for a long time in major international scientific initiatives [3], [13].

In addition to the building of the space instrument, it is necessary to improve the modeling of terrestrial surfaces as well as our understanding of the main signal contributors. It is in order to satisfy such goals that dedicated instruments were recently designed and built (the Passive Active L and S (PALS) [14], the ETH-L Band Radiometer (ELBARA) [15], to name but a few). For the preparation of SMOS, it is now necessary to start addressing new issues (special events) to validate root zone soil moisture estimation [16]. It is with this goal that the decision was taken to design, develop, and test an instrument dedicated to the analysis of: 1) special events such as frosts, dew, etc., and 2) to test and improve the algorithms used for estimating surface and root zone soil moisture from multiangular dual-polarized brightness temperatures measurements using assimilation techniques. To achieve this goal, a test site was selected near Toulouse and equipped with ground measurements over two surface types (bare soil and fallow grass). A large structure holding the L-band radiometer was erected and equipped with automatic pointing and data collection devices. In parallel, the L-Band Radiometer for Estimating Water in Soils (LEWIS) was designed, built, tested, and is now operational.

## II. TEST SITE DESCRIPTION

The outdoor measurements were carried out in a large experimental test site located near the town of Mauzac (43°28'N 1°19'E), south of Toulouse. This site belongs to the Office National d'Etudes et de Recherches en Aéronautique (ONERA) and has been chosen as a joint test facility called PIRRENE for “Programme Interdisciplinaire de Recherche en Radiométrie en ENvironnement Extérieur,” between the ONERA, the Centre d'Etudes Spatiales de la Biosphère (CESBio), and the Centre National de Recherche Météorologique (CNRM). Within this site, a large area was devoted to the SMOS preparation campaign where the LEWIS instrument was installed.

The site consists of a large area of fallow grass, of which a portion is kept in the state of bare soil. Right over the border between these two areas, a large structure (15 m high) has been erected on which the LEWIS radiometer is mounted (Fig. 1). From there, the radiometer is operated continuously to monitor

Manuscript received July 28, 2003; revised April 1, 2004. The funding for LEWIS was obtained through the Programme National Terre Atmosphere Ocean Biosphère of the Centre National d'Etudes Spatiales, while the Comité Consultatif Régional de la Recherche et du Développement Technologique of the Région Midi Pyrénées funded the ground setup.

F. Lemaître and J.-C. Poussière are with the Office National d'Etudes et de Recherches en Aéronautique, 31400 Toulouse, France.

Y. H. Kerr and P. de Rosnay are with the Centre d'Etudes Spatiales de la Biosphère, 31401 Toulouse Cedex 09, France.

M. Déjus is with the Centre National d'Etudes Spatiales, 31401 Toulouse Cedex 09, France.

R. Durbe and J.-C. Calvet are with Météo-France Centre National de Recherches Meteorologiques, 31057 Toulouse, France.

Digital Object Identifier 10.1109/TGRS.2004.831230



Fig. 1. LEWIS on its supporting structure and with rotating mechanism. The rotation axis is 13.6 m high. The length of LEWIS is 3 m, and the weight is about 200 kg.

the brightness temperatures as a function of time. LEWIS operates according to four different modes: The current scheme is as follows.

- 1) The most frequent is continuous observation of the grass plot at a constant  $40^\circ$  incidence angle.
- 2) The second mode takes place every 3 h (2:30, 5:30, 8:30, ..., 23:30 UT). It consists in scanning the two surfaces (bare soil and grass) at various angles around an east–west (E–W) axis ( $20^\circ$  to  $60^\circ$  incidence angles with a step of either  $5^\circ$  or  $10^\circ$ ). Fig. 2 shows a typical scan with two surface conditions obtained within a few hours before and after a rain event. Note that the scans were done twice (20 min apart) giving the two lines at H polarization for dry conditions.
- 3) The third nominal mode is sky pointing ( $45^\circ$  toward the north) for several hours to check the calibration through the evolution of the cold point at both polarizations. The time duration was selected to minimize signal discontinuities linked to the eventual (though not foreseen; considering existing maps) presence of galactic radio sources [17]. In other words, if a small radio source enters the beam, its apparent off-axis movement may cause a momentary perturbation, with a 24-h period.
- 4) In case of anomalies and of strong winds, there is finally a special position with LEWIS pointing directly below and being automatically bolted to the structure. The system was submitted to large gale events in March and April (hence some data gaps), but the security worked very nicely.

The system is designed to enable changing the measurement routine as well as enabling manual positioning of the system for specific sets of measurements.

On the ground various other measurements are performed, replicating the Monitoring the Usable soil Reservoir Experimentally (MUREX) setup [18]. For the whole area, flux and radiation

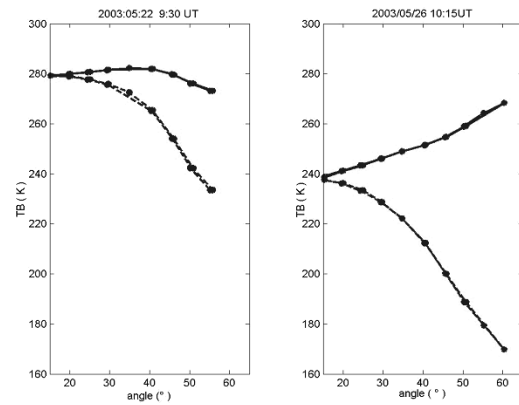


Fig. 2. Angular variations of the brightness temperature over the same plot (bare soil) for (left) dry conditions and (right) a few hours later after a rain event.

measurements are performed (see MUREX list), and two trenches (one in each plot, i.e., grass and bare soil) were equipped with moisture and temperature profiles. Additionally, the vegetation biomass is monitored weekly on the grass site through direct measurements, and surface moisture is measured continuously.

Data are automatically recorded on computers and transmitted to either CESBIO ONERA or CNRM through a phone line for analysis, processing, and archiving.

### III. LEWIS: SYSTEM DESCRIPTION

The system consists of an L-band antenna with radio-frequency (RF) parts positioned around the wave-guide section, as shown in Fig. 3. This section is thermally regulated, and hence, a cylindrical thermal-isolated cap covers it.

In order to ensure a high differential accuracy for the H and V brightness temperatures, it was decided not to use the classical noise-injection design so as to avoid the necessary couplers, since their long-term differential behaviors are questionable. Our design, as shown in Figs. 3 and 4, uses a four-channel Dicke switch at the input of the RF receiver, which sequentially processes the four signals (namely, antenna ports H and V, reference load, noise). After detection, three synchronous demodulators (SD1, SD2, and SD3) are used to cancel the receiver noise contribution and deliver three voltages  $U_H$ ,  $U_V$ , and  $U_D$  as detailed below. Fig. 4 depicts the temporal gain sequence used for the demodulators

$$\begin{aligned}
 U_H(t) &= G(t) \cdot (T_H - T_L) \\
 U_V(t) &= G(t) \cdot (T_V - T_L) \\
 U_D(t) &= G(t) \cdot (T_D - T_L)
 \end{aligned} \tag{1}$$

where

- $T_L$  brightness temperature of the reference load;
- $T_H$  antenna horizontal brightness temperature;
- $T_V$  antenna vertical brightness temperature;
- $T_D$  noise diode brightness temperature;
- $G(t)$  instantaneous receiver gain.

Due to small gain fluctuations generated by flicker noise in the receiver, the gain  $G(t)$  has to be considered as noisy with a typical time constant of 1 Hz. Its instantaneous value is then computed from the measured  $U_D(t)$  and the known parameters  $T_D$  and  $T_L$ , allowing the computation of  $T_H$  and  $T_V$  using (2) as detailed below.

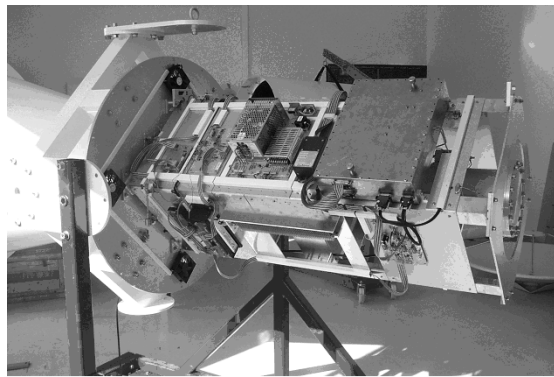
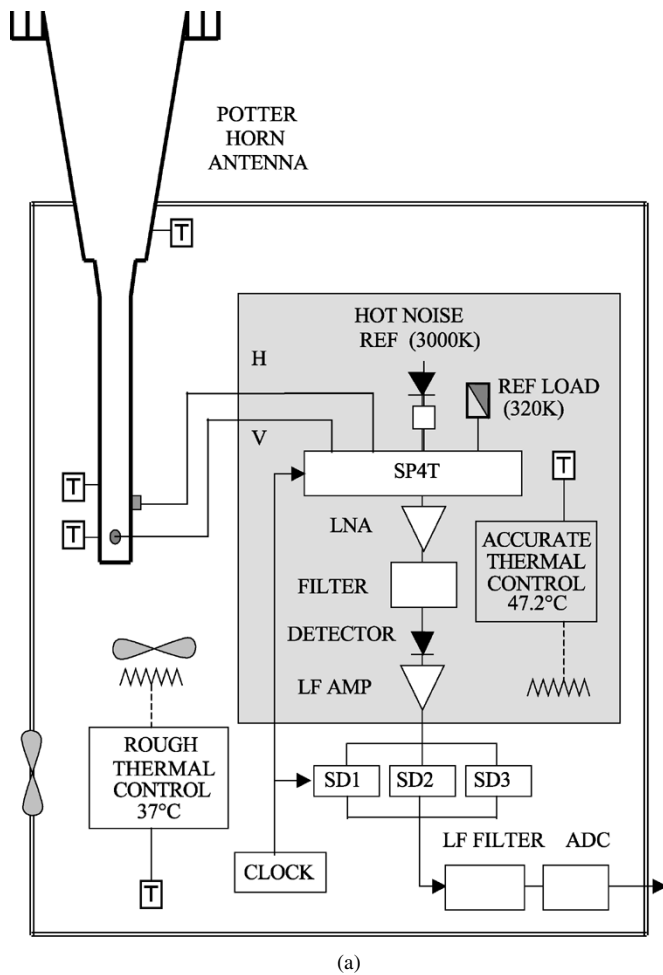


Fig. 3.(a) Overall system block diagram. Thermocouples are indicated by the letter "T." Refer to text for the other letters. The shaded area corresponds to the large copper block shown in (b) (receiver). The four-channel switch selects sequentially the antenna outputs and the two temperature references at the input of the receiver. After amplifying and filtering, the detected signal is then processed with three synchronous demodulators (SD1, SD2, and SD3) that subtract the reference load brightness and the receiver intrinsic noise. The three filtered outputs represent, respectively, the H and V antenna brightness and the instantaneous gain of the receiver. (b) Inside of the instrument (cylindrical cover removed). The details of the electronic and electrical circuitry inside LEWIS are visible. Note the large copper structure (the heart of the receiver), containing all the RF circuits, and which temperature is controlled within  $\pm 0.02$  °C. The air inside the cover is continuously stirred by a fan and regulated at 37 °C.

The Dicke design allows canceling the receiver's gain variations, except for the losses due to the waveguide-to-coaxial transitions and losses of the coaxial cable linking the antenna to the

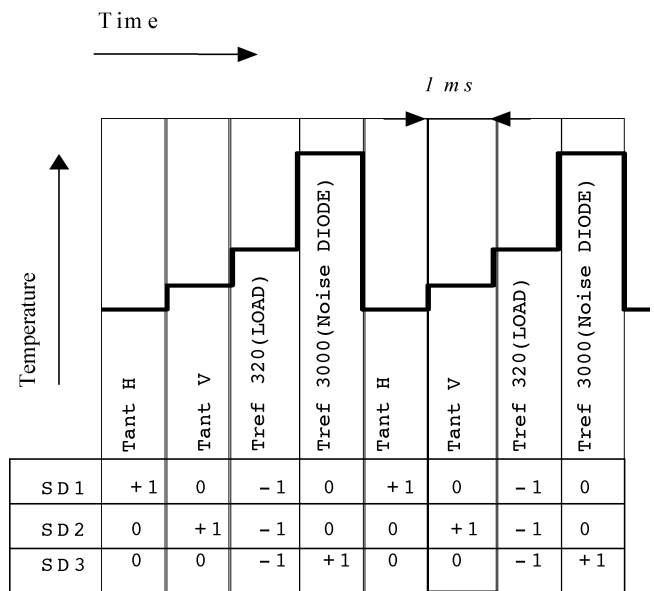


Fig. 4. Temporal diagram showing the time sharing of the receiver and the associated gain in the synchronous demodulators.

RF receiver. The noise contribution is slightly increased by the latter, the level of noise being a function of their temperatures, which cannot be well controlled due to the antenna temperature variations (the antenna itself is at air temperature). It is worth noting that for a cable attenuation  $a$  of 0.1 dB at  $T = 300$  K, the contribution generated is of  $(1 - a) * T = 6.7$  K. Consequently, the temperatures along these paths are monitored to enable further compensation. The three radiometric signals and temperature measurements are converted and sent every 2 s to a desktop computer through an RS485 link.

All the compensations (switch isolations, offsets, gain variations, cable radiations, etc.) and calibration are performed later by software.

### A. Antenna

The antenna characteristics are certainly of utmost importance for a high-quality L-band radiometer. Due to the small relative bandwidth, and for mechanical considerations, a Potter horn design was chosen. The device is composed of a 90-cm-long circular wave-guide followed by two conical sections separated by the Potter discontinuity. Corrugations around the 1.3-m diameter aperture were added to lower the sidelobe levels. The dimensions were carefully optimized to achieve the best antenna performances (sidelobe levels, H/V symmetry, beam efficiency), with the smallest possible dimensions, and the lowest sensitivity to mechanical inaccuracy or thermal deformations across all the bandwidth ( $1414 \pm 10$  MHz). The computed pattern at 1414 MHz presented on Fig. 5 shows a  $13.6^\circ$  3-dB beamwidth and first sidelobes as low as  $-38$  dB. The calculated beam efficiency (relative power in  $2.5 * \text{HPBW}$ ) is greater than 98%.

### B. RF Design

The RF front end includes a PIN diode SP4T switch (insertion loss (IL)  $< 0.5$  dB) followed by a low-noise amplifier

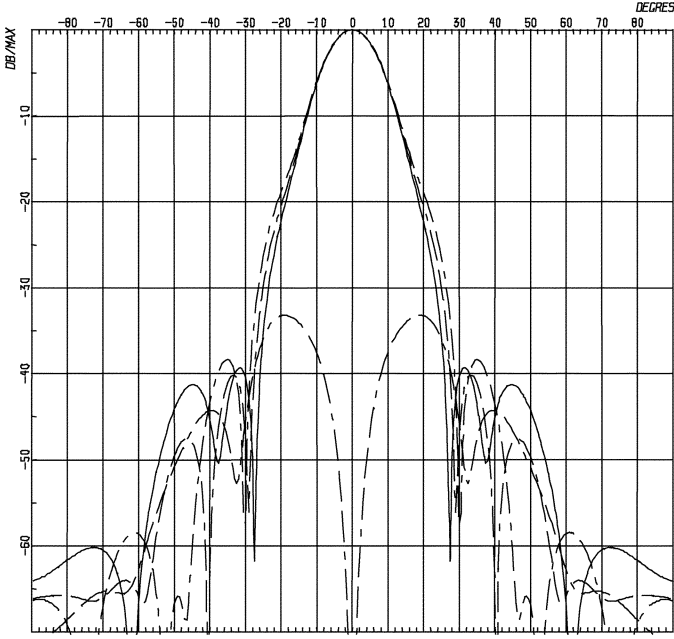


Fig. 5. Computed antenna pattern of the Potter horn [21], showing very low sidelobes. Note that  $24^\circ$  from the beam axis, the antenna gain is different for the H and V polarization ( $-32$  dB in H-pol and  $-25$  dB in V-pol). (Dashed dotted line)  $0^\circ$  plane (V). (Dashed line)  $45^\circ$  plane. (Solid line)  $90^\circ$  plane (H).

(noise factor (NF) = 0.35 dB). In order to protect as far as possible the system from radio-frequency interference (RFI), the receiver bandwidth is limited by a 12-pole cavity filter. Other amplifiers (not shown in Fig. 3) are used to set the RF noise level at the detector input in the range ( $-35$  dBm,  $-25$  dBm).

### C. Temperature Regulation

All of the RF parts are housed in a copper box 30 cm wide, with 8-mm wall thickness (weight  $\sim 30$  kg), accurately regulated at  $47.2^\circ\text{C}$ . In order to achieve stable external conditions for this thermal regulation, the air inside the cover and around the receiver in the cylindrical cover is stirred by two fans and regulated at  $37^\circ\text{C}$ . These temperatures were chosen high so that even in case of hot weather thermal regulation can be achieved by means of heating only. In case of very hot weather, four fans are automatically powered to force internal/external air exchanges. The thermal equilibrium/temperature regulation is achieved after 2 h. During the rather hot 2003 summer (surface temperature reached  $60^\circ\text{C}$ ), the whole system behaved quite nicely. Temperature variations measured with a platinum probe close to the RF load stay within  $\pm 0.02^\circ\text{C}$  of the targeted  $47.2^\circ\text{C}$ . Two short low-loss semirigid cables are used to link the antenna outputs H and V to the RF receiver. Temperatures at their antenna ends are monitored for compensation.

### D. Calculated Performances

From (1), the brightness temperature at the antenna output  $T_A$  ( $A = \text{H or V}$ ) is obtained by

$$G(t) = \frac{U_D(t)}{T_D - T_L} \quad T_A = T_L + \frac{U_A(t)}{G(t)} = T_L + \frac{U_A(t)}{U_D(t)} \cdot (T_D - T_L). \quad (2)$$

As  $U_A$  and  $U_D$  are measured practically at the same time, their ratio is independent of  $G(t)$  fluctuations. The voltages

$U_A$  and  $U_D$  have the general properties of detected RF noise: their mean values equal their standard deviations. After low-frequency filtering, the ratio of those quantities is improved by a factor equal to the square root of the number of the equivalent independent observations [19]. Then, the standard deviation of a detected and filtered RF noise is

$$\sigma(U) = \frac{\langle U \rangle}{\sqrt{B\tau f}} \quad (3)$$

where

- $\langle \rangle$  “average value of”;
- $B$  RF bandwidth before detection;
- $\tau$  equivalent integration time of the postdetection filter;
- $f$  time duty factor of the receiver for the considered signal (here  $f = 0.25$ ).

The outputs of synchronous demodulators can be considered as the difference of two independent signals having the statistical properties mentioned above and containing the contribution of the receiver noise  $T_R$ . So, the standard deviations of  $U_A$ ,  $U_D$  and the ratio  $U_A/U_D$  can be computed

$$\begin{aligned} \sigma(U_D) &= G(t) \frac{\sqrt{(T_R + T_L)^2 + (T_R + T_D)^2}}{\sqrt{B\tau f}} \\ \sigma(U_A) &= G(t) \frac{\sqrt{(T_R + T_L)^2 + (T_R + T_A)^2}}{\sqrt{B\tau f}} \\ \sigma\left(\frac{U_A}{U_D}\right) &= \frac{\langle U_D \rangle \sigma(U_A) + \langle U_A \rangle \sigma(U_D)}{\langle U_D \rangle^2} \\ &= \frac{\sigma(U_A)}{\langle U_D \rangle} + \frac{\langle U_A \rangle \sigma(U_D)}{\langle U_D \rangle^2}. \end{aligned} \quad (4)$$

Combining (2) and (4), and considering the two independent contributions coming from the measurements of  $T_L - T_A$  and  $T_L - T_D$ , respectively, the standard deviation  $\sigma(T_A)$  can be expressed as

$$\sigma(T_A) = \sqrt{\sigma^2(T_{AA}) + \sigma^2(T_{AG})} \quad (5)$$

where

$$\sigma(T_{AA}) = \frac{\sqrt{(T_R + T_A)^2 + (T_R + T_L)^2}}{\sqrt{B\tau f}} \quad (6)$$

$$\sigma(T_{AG}) = |T_A - T_C| \frac{\sqrt{(T_R + T_D)^2 + (T_R + T_L)^2}}{(T_D - T_L)\sqrt{B\tau f}}. \quad (7)$$

The parameter  $T_D$  must be high enough to give a good accuracy for the gain measurement and small enough to avoid linearity problems with the detector. Fig. 6 shows that with the choice  $T_D = 3000$  K, and for the mentioned values of the other parameters, a nearly constant sensitivity of 0.2 K is obtained over the  $[0 \text{ K}, 300 \text{ K}]$  range.

## IV. CALIBRATION

### A. Receiver Calibration

All the unavoidable defects of the receiver were measured and whenever possible accounted for by software. These include imperfect switch isolations, demodulator leakage due to the limited bandwidth of the low-frequency processed signals, offsets, etc.

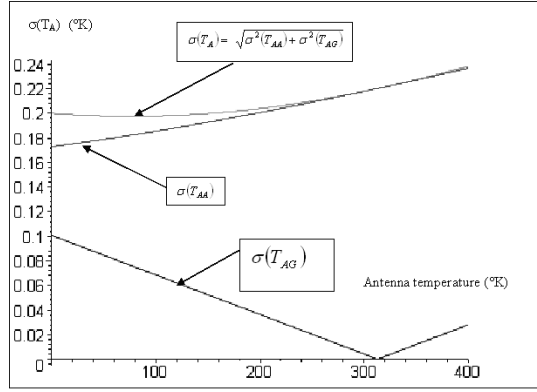


Fig. 6. Computed  $\sigma(T_A)$  with  $\{T_R = 280 \text{ K}, T_L = 320 \text{ K}, \text{ and } T_D = 3000 \text{ K}; B = 15 \text{ MHz}, \tau = 4 \text{ s}, f = 0.25\}$  is quite constant over the range  $[0 \text{ } 300 \text{ K}]$ . The  $\sigma(T_{AG})$  contribution comes from the noise in the measurement of the instantaneous gain  $G(t)$ . The  $\sigma(T_{AA})$  term is due to the noise in the measurement of  $T_A - T_L$ .

The receiver was calibrated using two classical methods: the first one relies on the use of RF loads at ambient or in liquid nitrogen, while the second one uses an external noise source and an attenuator. The two approaches delivered very similar results within  $\pm 2 \text{ K}$ .

### B. Receiver Linearity

As the detector is used over a large range of approximately 10 dB, nonlinearity must be investigated. This was done first by considering a nonlinear detector model (8) involving the quadratic parameter  $b$ . Note that the receiver noise contribution  $T_R$  has to be taken into account in this model

$$U = G((T_R + T) + b(T_R + T)^2). \quad (8)$$

Using this new expression of  $U$  in (2), the estimated incident temperature  $T_{A\_est}$  can be calculated taking into account the effective the ratio  $U_A/U_D$

$$T_{A\_est} = T_L + (T_D - T_L) \frac{T_A - T_L + b(T_R + T_A)^2 - b(T_R + T_L)^2}{T_D - T_L + b(T_R + T_D)^2 - b(T_R + T_L)^2}. \quad (9)$$

The error introduced by the nonlinearity is then obtained after some calculations

$$T_{A\_est} - T_A = \frac{(T_L - T_A)(T_D - T_A)b}{1 + b(T_D + T_L + 2T_R)}. \quad (10)$$

The setup used for the measurement of the  $b$  parameter is presented in Fig. 7. The principle consists of adding an identical amount of power in the lower and the higher domain of the receiver dynamic range. Parameter  $b$  can, therefore, be identified by the difference between the differences  $\Delta T_{az}$  and  $\Delta T_{am}$ . These measurements are particularly difficult to achieve due to: 1) the small value of the mentioned difference (1–3 K); and 2) temperature variations in the laboratory and of the coaxial cable. For these reasons, a copper mass was added to prevent the coupler from cooling when the RF load is in the liquid nitrogen.

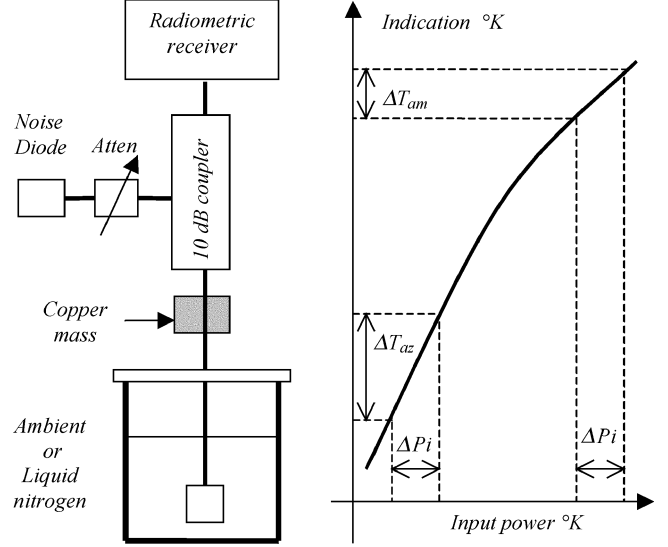


Fig. 7. Receiver linearity characterization setup. It consists in injecting a calibrated power increment  $\Delta P_i$  in the lower and the upper area of the dynamic range of the receiver and comparing the produced response at the output of the receiver. The nonlinear parameter  $b$  is derived from these measurements.

Using this method, we found the  $b$  parameter to be equal to  $5.10^{-6}$ . This value leads to a maximum nonlinearity error of 0.15 K in the range  $[0 \text{ K}, 300 \text{ K}]$  after the overall calibration.

### C. Overall System Calibration

The RF matching conditions at the ends of the cables linking a hot source to the receiver influences the power transfer and thus introduces uncertainty. Even under relatively good matching conditions (return losses  $< -20 \text{ dB}$ ), modifications in the length of the cables can modify the matching conditions and lead to errors of up to several kelvin in the measurements. The calibration has, thus, to be complemented with an end-to-end calibration consisting in setting the instrument successively in front of two specific, well-known targets, a hot and a cold one.

However, before performing this task, the contribution of the wave-guide-to-coax transition and of the coaxial cable linking them to the receiver must be taken into account as mentioned before. This is mainly due to the fact that their temperatures cannot be totally controlled. Compensation coefficients were, thus, identified by aiming the radiometer to the celestial north and warming “quickly” the end of the waveguide with a heater.

The “warm” target situation obtained in an anechoic chamber at the Centre National d’Etudes Spatiales ( $22 \times 12 \times 12 \text{ m}^3$ ), the temperature of which is very well controlled ( $\pm 0.2 \text{ }^\circ\text{C}$ ), and in which two 12-h records were completed.

The “cold” scene was the sky, which has a much more complex behavior. At L-band, the radiometric brightness of the sky depends on the elevation angle of the antenna, weather conditions, and also on the presence (or not) of radio sources in the antenna beam. A large number of radio sources are located in the Milky Way. Fig. 11 shows the setup used for sky calibration.

To be certain that contributions from the ground remains small ( $< 0.2 \text{ K}$ ), we chose to make this calibration at  $60^\circ$  and  $90^\circ$  elevation angles. The drawback of this choice is sky temperature variations with the sidereal time. According to

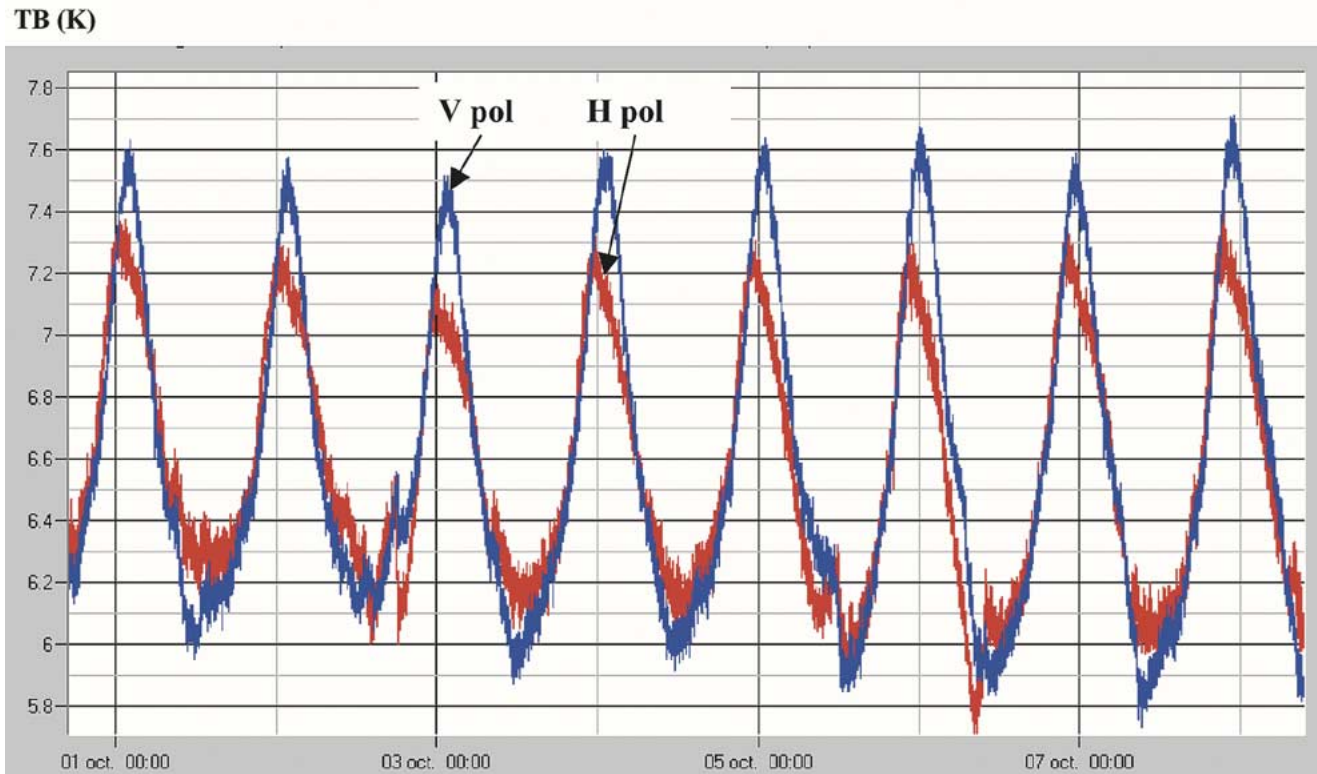


Fig. 8. Seven-day record at  $60^\circ$  elevation angle taken in October 2002.

Delahaye's paper [17], the galactic background is composed of a radio continuum to which several "bright" regions are superimposed, due to emissions from discrete radio sources. The galactic radiation has a maximum spread toward the galactic center and a strong emission ribbon close to the galactic equator, with a strong maximum close to the galactic center, and another significant radio source named "Cygnus A." Besides, the neutral atomic hydrogen emission line (HI) at 1420.406 MHz has to be taken into account. Delahaye used these two contributions for the calculation of the brightness temperature seen by a  $15^\circ$  antenna instrument by double angular integration. The result is a minimum of 3.9 K in the direction of the galactic north.

So, the sky radiometric temperature at  $60^\circ$  varies in the range [5.6 K, 7.0 K] with the following contributions:

- galactic background:*  $3.9 \pm \text{K}$  (time dependent);
- atmospheric attenuation:*  $2.3 \pm 0.2 \text{ K}$  (weather dependent);
- estimated ground contribution:* 0.1 K.

Figs. 8 and 9 show the results after having set the "best" calibration parameters. It can be seen that  $90^\circ$  elevation records are much more difficult to interpret because the antenna beam crosses twice a day the Milky Way, and the sun is nearby the beam axis (at  $24^\circ$  from it) at noon. The asymmetry in the corresponding relative level in the H/V antenna pattern at this angle (see Fig. 5) explains why the H channel collects ten times more power from it than the V channel in this situation. In the same way, some asymmetrical distribution of galactic radio sources in the antenna beam could explain the 0.3-K observed difference for maximum values in Fig. 8. For these reasons, mostly the observed minima were taken into account for the sky calibration process.

After measurements over several days, and taking into account the galactic background and atmospheric contribution uncertainties, the absolute calibration accuracy is estimated at 0.5 K.

#### D. Long-Term Stability

The long-term stability depends on many factors, mainly the stability of RF parameters over long time periods. Among them, loss variations of some coaxial link as low as 0.01 dB can produce 1-K errors in the results.

During the first month of use of LEWIS, a drift appeared with a characteristic exponential shape (time constant approximately five days). The cause of this drift is generally considered to be related to a strength relaxation process of the dielectric material inside the coaxial link. After this period of time, a regular and quite constant slope of 0.6 K/month was observed. The cause of this drift was identified to be linked to the evolution of the ENR (excess noise ratio) parameter of the noise diode. Consequently, an evolution model of this drift (0.000 25 dB/day) was added, and the result presented Fig. 10 was obtained. The remaining variations are compatible with the  $\pm 0.2$ -K weather dependency mentioned above. Fig. 10 also shows the good long-term stability of the difference of H and V brightness. The two big peaks (indicated by arrows) in this figure are due to the RF radiation of lightning flashes.

## V. FIRST RESULTS: SOME EXAMPLES

After initial testing and calibration as depicted above, the instrument was mounted on a specially erected 15-m-high structure (Fig. 1). The elevation angle is motor controlled in the vertical north-south plane. It allows periodic aiming at the sky, which is useful for checking calibration.

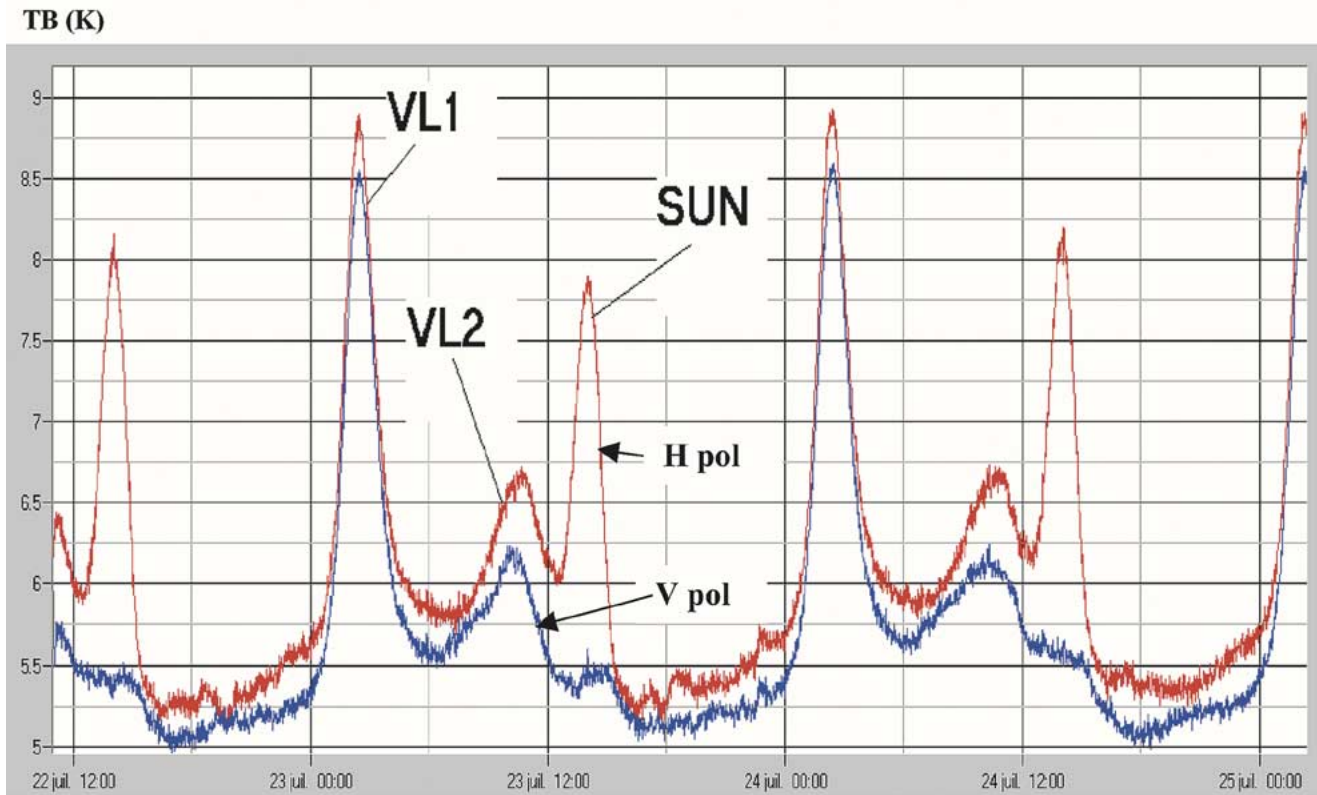


Fig. 9. Three-day record at  $90^\circ$  elevation angle taken in July 2002. VL1 and VL2 correspond to the Milky Way crossing the beam. Due to asymmetry of the H and V antenna pattern at  $24^\circ$  from the axis, the sun is mainly visible in H polarization.

The first results depicted here are simply to illustrate some of the measurements performed by LEWIS. It is not our goal to analyze in details the results in this paper but rather to illustrate the instrument performances.

#### A. Monthly Trends

LEWIS started making acquisitions at the end of January 2003 and has been making continuous measurements, save for periods of strong winds and for two periods when the automatic positioning system jammed.

Fig. 12 shows a drying-out sequence obtained in March 2003. The top figure shows the temporal evolution of emissivity. Note the diurnal cycle and the data gap (DOY 81–84) when a power failure caused a severe data loss (LEWIS Acquisition computer was down on DOY 81–82) and altered the dates of the data logger (meteorological and ground data) causing an overwrite (DOY 83–84). The second plot shows the temporal evolution of the polarization ratio PR [20] for a  $20^\circ$  incidence angle

$$PR = \frac{(T_{Bv} - T_{Bh})}{(T_{Bv} + T_{Bh})}. \quad (11)$$

The correlation with surface soil moisture as indicated in the bottom figure is quite striking even though the depolarization is quite small ( $20^\circ$  incidence angle), showing the good performances of LEWIS. The sudden dip in the surface soil moisture measurements on DOY 74 is not yet explained. It occurs on both plots (fallow and bare soil) but only for the surface probes.

Fig. 13 shows very similar curves but obtained here at  $40^\circ$  incidence angle and during the month of April during a series of rain

events. Both bare soil and vegetation covered surfaces are plotted. At this period of the year, the grass starts its growth cycle. The measured total fresh biomass (including green and litter) for a dry (i.e., no rain) period reaches  $700 \text{ g/m}^2$  with a 45% water content. After precipitation events, the total biomass measurements show an increase to  $1000 \text{ g/m}^2$  with a 60% water content. The impact of rain events on the brightness temperature is quite obvious. Looking at the polarization ratio curves, one may notice very different tendencies for bare soil and vegetation. Over bare soils, the brightness temperatures (and PR) react immediately to the increase of soil moisture after a rain, to decrease slowly afterward as the surface dries out. Over the grass, the temporal evolution of the signal is more complex. First, due to interception, the ground gets less water; second, rain intercepted increases significantly the vegetation water content and hence reduces the polarization ratio. Finally, the vegetation tends to accumulate water (especially in the litter), which will only dry slowly. Actually, over our fallow plot, the litter is significant, and several centimeters of dead vegetation makes a distinctive layer between the vegetation layer and the soil itself. This layer tends to accumulate water (similar to a sponge) and behave like a blackbody when wet. Afterward, it dries out more quickly than the soil underneath, and the polarization ratio increases. This explains the temporal evolution of the curves in Fig. 13.

#### B. Freezing Events

Just after LEWIS was installed, we were lucky enough to capture several light freezing events in February. Over the bare soil plot due to the lack of vegetation, the surface froze lightly

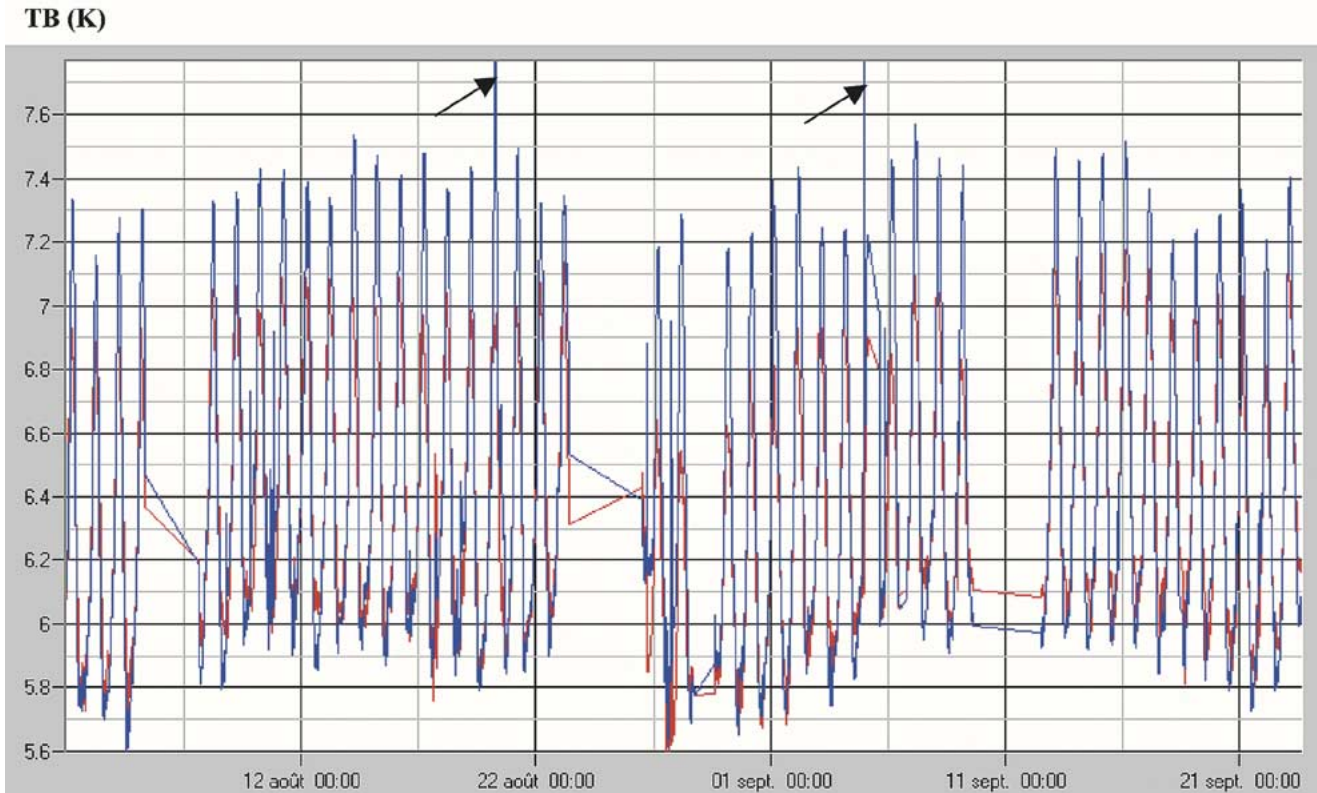


Fig. 10. Fifty-day record at  $60^\circ$  elevation angle. Red and blue curves stand, respectively, for H polarization and V polarization. Note the overall stability of the signal as well as the diurnal cycle (galactic background heterogeneity) and atmospheric effects.



Fig. 11. Overall calibration using the sky. The plastic foil was implemented to protect the instrument (always pointing toward the sky for several months) so as to avoid collecting rain through the horn. Specific measurements showed that as long as the plastic did not fill up with a significant amount of water, and as long as water did not gather in small top-to-bottom rivulets, the impact of this improvised radome could not be measured in the collected data.

(the probes located at  $-5$  cm indicated slightly positive temperature (274.2 K) but interpolation to 1-cm depth validated with September 2003 data gives a slightly negative temperature (272.2 K on DOY 37.19 as shown in Fig. 14), while over the grass plot temperature at the soil's surface remained above 273 K. This is easily visible on the soil moisture plots with artificial (frozen means no liquid water hence the probes give lower soil moisture

values) soil moisture decreases in the bare soil curve, correlated to low temperatures from early to mid morning. Accordingly, brightness temperatures over bare soil increase simultaneously (change of dielectric constant due to freezing). Conversely, over the grass-covered area, the soil does not freeze, while vegetation freezes slightly, becoming more transparent. So, the radiometer sees a higher proportion of soil signal that has a lower emissivity and, hence, the decrease in brightness temperature. It is worth noting the significant change of slope of the vegetation brightness temperature at sunset and sunrise.

These examples are just given to show the degree of detail that can be accessed with such a setup, while data interpretation and modeling will be described in papers to come. The important fact is that LEWIS can detect and monitor very fine events. The first weeks of operation also allowed capturing the impact of heavy rain and subsequent interception on the signal as well as a fine monitoring of water stratification within the soil and canopy during a diurnal cycle.

## VI. CONCLUSION

A precision L-band dual-polarization radiometer has been designed calibrated and tested. It uses an original architecture that ensures a good accuracy for the differential brightness temperature  $T_V - T_H$ . The nonlinearity of the system was measured and was found lower than the instrument resolution equal to 0.2 K for a 4-s integration time. The high-quality antenna (low side-lobes and cross-polarization isolation) ensures good reliability of the measurements. Experimental aspects of calibration using the sky as a cold situation was presented and discussed. The estimated absolute accuracy of the calibration of the instrument is

### SMOSREX measurements on bare soil February 2003

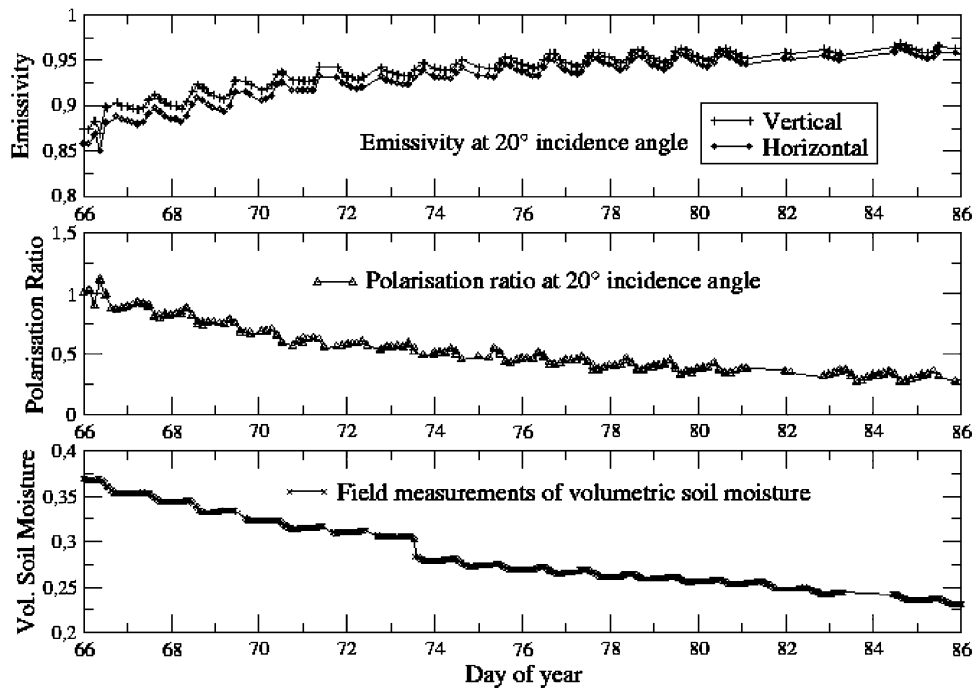


Fig. 12. Drying sequence (bare soil only) during the month of March 2003. Data gaps were caused by a general power failure (see text). The  $x$  axis is the day of year (DOY) 2003. (Top) Emissivity plots. (Middle) Polarization ratio (multiplied by  $10^4$ ) and both at  $20^\circ$  incidence angle. (Bottom) Volumetric soil moisture (percent) as measured by a “surface” probe (i.e., 3–5 cm).

### SMOSREX measurements on fallow and bare soil April 2003

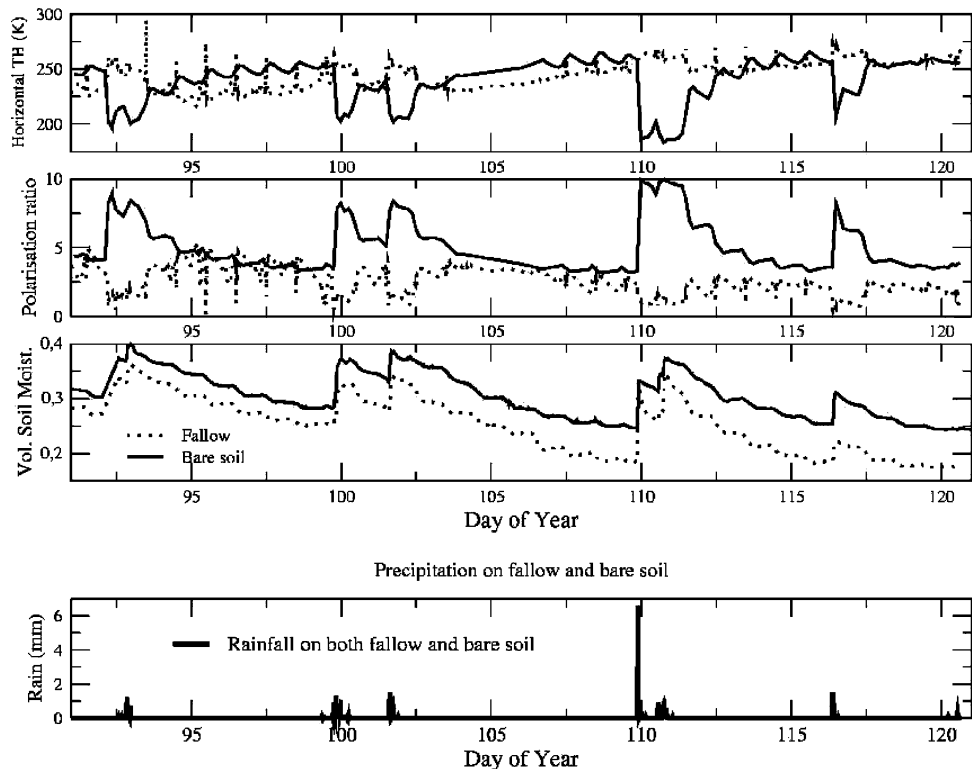


Fig. 13. Impact of the occurrence of rain events during the month of April 2003. The  $x$  axis is DOY 2003. (Top) Brightness temperatures (K) at the incidence of  $40^\circ$  at H polarization (bold bare soil, dotted fallow). (Top middle) Polarization ratio  $\times 10^4$  (fallow dotted, bare soil bold). (Bottom middle) Volumetric soil moisture (percent) (bold bare soil, dotted fallow). (Bottom) Rainfall amounts (millimeters).

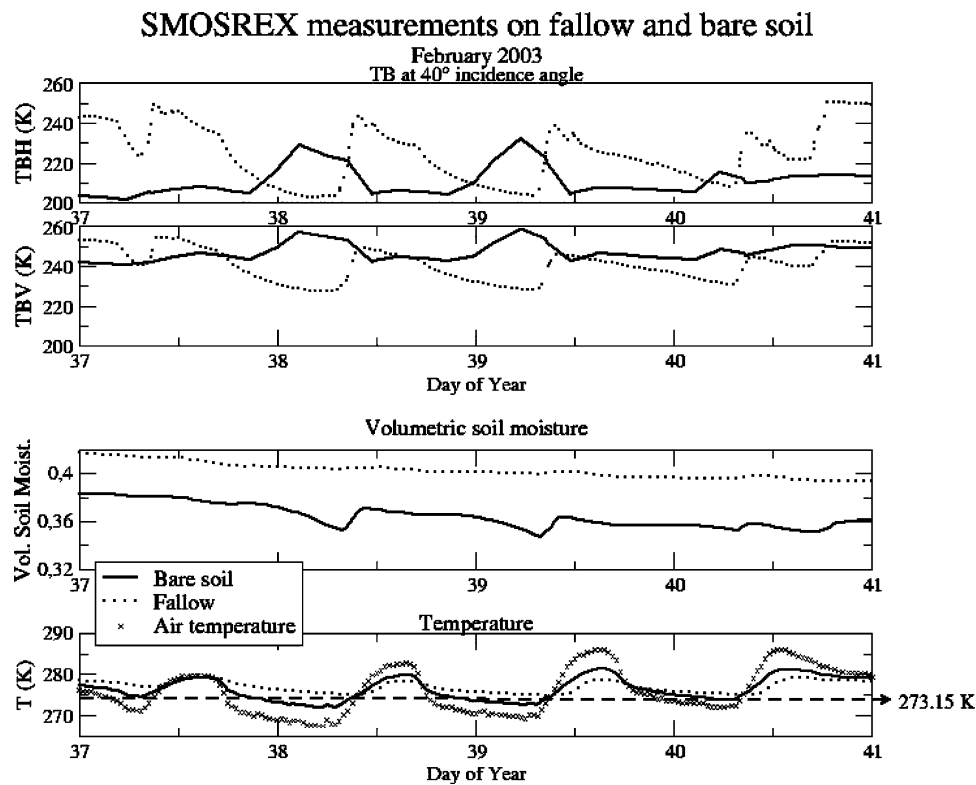


Fig. 14. Light surface freezing conditions as seen at an incidence of  $40^\circ$ ,  $x$  axis DOY 2003. (Top) Horizontal brightness temperatures: (K) dotted, fallow, bold bare soil. (Top middle) Vertical brightness temperatures: (K) dotted, fallow, bold bare soil. (Bottom middle) Volumetric soil moisture (percent) bold bare soil, dotted fallow. (Bottom) Near-surface temperature ( $-1$  cm) bold bare soil, dotted fallow, "\*" air temperature (K). Dashed line gives the freezing temperature  $0^\circ\text{C}$ .

0.5 K. The long time stability demonstrated with a 50-day monitoring, taking into account a drift of the ENR noise diode, is estimated to be as low as  $0.3\text{ K/month}$ .

The first measurements showed that LEWIS is sensitive enough to detect a very distant radio source (Cygnus A) and even to put in evidence a very probable polarized signal from radio sources. Concerning the field application of LEWIS, the system has worked perfectly for over one year now, enabling the yield of a wealth of measurements with a wide range of surface conditions, with an unprecedented accuracy. We can now monitor in detail the evolution of the brightness temperatures of natural surfaces, as well as sporadic events such as light freezing, heavy rainfall or extreme heat, because of the instrument's ability to make measurements with high temporal resolution over long periods of time and very different environmental conditions.

#### ACKNOWLEDGMENT

The authors are very grateful to the CNRM-4M team who implemented LEWIS on the site and M. J. Escorihuela for making part of the LEWIS data processing algorithms. They wish to thank P. Waldteufel, J. Yves Delahaye, and J.-P. Wigneron for fruitful discussions. They are also very thankful to the anonymous reviewers for their very useful comments.

#### REFERENCES

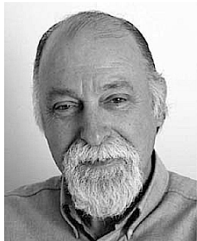
- [1] P. A. Dirmeyer, "Assessing GCM sensitivity to soil wetness using GSWP data," *J. Meteorol. Soc. Jpn.*, vol. 77, pp. 367–385, 1999.
- [2] D. Entekhabi and P. S. Eagleson, "Climate and the equilibrium state of land surface hydrology parameterizations," *Surv. Geophys.*, vol. 12, pp. 205–220, 1991.
- [3] D. Entekhabi, G. R. Asrar, A. K. Betts, K. J. Beven, R. L. Bras, C. J. Duffy, T. Dunne, R. D. Koster, D. P. Lettenmaier, D. B. McLaughlin, W. J. Shuttleworth, M. T. van Genuchten, M. Y. Wei, and E. F. Wood, "An agenda for land surface hydrology research and a call for the second international hydrological decade," *Bull. Amer. Meteorol. Soc.*, vol. 80, pp. 2043–2058, 1999.
- [4] E. G. Njoku and D. Entekhabi, "Passive microwave remote sensing of soil moisture," *J. Hydrol.*, vol. 184, pp. 101–129, 1996.
- [5] Y. H. Kerr and T. J. Jackson, "Working group report on soil moisture," in *Passive Microwave Remote Sensing of Land-Atmosphere Interactions*, P. Pampaloni, Ed. Zeist, The Netherlands: VSP, 1995, pp. 661–667.
- [6] T. Schmugge, "Applications of passive microwave observations of surface soil moisture," *J. Hydrol.*, vol. 212–213, pp. 188–197, 1998.
- [7] E. G. Njoku and L. Li, "Retrieval of land surface parameters using passive microwave measurements at 6–18 GHz," *IEEE Trans. Geosci. Remote Sensing*, vol. 37, pp. 79–93, Jan. 1999.
- [8] Y. H. Kerr, P. Waldteufel, J.-P. Wigneron, J.-M. Martinuzzi, J. Font, and M. Berger, "Soil moisture retrieval from space: The Soil Moisture and Ocean Salinity (SMOS) mission," *IEEE Trans. Geosci. Remote Sensing*, vol. 39, pp. 1729–1735, Aug. 2001.
- [9] P. Silvestrin, M. Berger, Y. H. Kerr, and J. Font, "ESA's second earth explorer opportunity mission: The Soil Moisture and Ocean Salinity mission—SMOS," *IEEE Geosci. Remote Sensing Newslett.*, vol. 11–14, 2001.
- [10] D. M. LeVine, A. J. Griffis, C. T. Swift, and T. J. Jackson, "ESTAR: A synthetic aperture microwave radiometer for remote sensing applications," *Proc. IEEE*, vol. 82, pp. 1787–1801, Dec. 1994.
- [11] D. M. LeVine, "Synthetic aperture radiometer systems," *IEEE Trans. Microwave Theory Tech.*, vol. 47, pp. 2228–2236, Dec. 1999.
- [12] F. Bayle, J.-P. Wigneron, Y. H. Kerr, P. Waldteufel, E. Anterrieu, J.-C. Orhlac, A. Chanzy, O. Marloie, M. Bernardini, S. Sobjaerg, J.-C. Calvet, J.-M. Goutoule, and N. Skou, "Two-dimensional synthetic aperture images over a land surface scene," *IEEE Trans. Geosci. Remote Sensing*, vol. 40, pp. 710–714, Mar. 2002.
- [13] *Proc. GEWEX/BAHC Int. Workshop Soil Moisture Monitoring, Analysis Prediction for Hydrometeorological Hydroclimatological Applications*, vol. 35, Univ. Oklahoma, Norman, OK, May 16–18, 2000.

- [14] W. J. Wilson, S. H. Yueh, J. Dinardo, S. L. Chazanoff, A. Kitiyakara, F. K. Li, and Y. Rahmat-Samii, "Passive Active L and S Band (PALS) microwave sensor for salinity and soil moisture measurements," *IEEE Trans. Geosci. Remote Sensing*, vol. 39, pp. 1039–1047, May 2001.
- [15] C. Mätzler, D. Weber, M. Wthrich, K. Schneeberger, C. Stamm, H. Wydler, and H. Flüher, "ELBARA, the ETH L-BAND radiometer for soil moisture research," in *Proc. IGARSS*, Toulouse, France, 2003.
- [16] J.-C. Calvet and J. Noilhan, "From near surface to root zone soil moisture using year round data," *J. Hydrometeorol.*, vol. 1, pp. 393–411, 2000.
- [17] J.-Y. Delahaye, P. Golé, and P. Waldteufel, "Calibration error of L-band sky-looking ground-based radiometers," *Radio Sci.*, vol. 37, pp. 11/1–11/11, 2002.
- [18] J. C. Calvet, P. Bessemoulin, J. Noilhan, C. Berne, I. Braud, D. Courault, N. Fritz, E. Gonzalez-Sosa, J. P. Goutorbe, R. Haverkamp, G. Jaubert, L. Kergoat, G. Lachaud, J. P. Laurent, P. Mordelet, A. Olioso, P. Peris, J. L. Roujean, J. L. Thony, C. Tosca, M. Vauclin, and D. Vignes, "MUREX: A land-surface field experiment to study the annual cycle of the energy and water budgets," *Ann. Geophys.—Atmos. Hydrosph. Space Sci.*, vol. 17, pp. 838–854, 1999.
- [19] F. T. Ulaby, R. K. Moore, and A. K. Fung, *Microwave Remote Sensing—Active and Passive*. Norwood, MA: Artech House, 1981, vol. 1.
- [20] Y. H. Kerr and E. G. Njoku, "A semiempirical model for interpreting microwave emission from semiarid land surfaces as seen from space," *IEEE Trans. Geosci. Remote Sens.*, vol. 28, pp. 384–393, May 1990.
- [21] M. Dejus, Modélisation d'un cornet de Potter pour l'ONERA dans le cadre du projet SMOS, in CNES DTS/AE/TTL/AN, Toulouse, France, 2000.



**François Lemaître** was born in France in 1957. He received the Eng. degree in electronics from the Ecole Nationale Supérieure des Arts et Métiers de Paris (ENSAM), Paris, France, in 1977.

He joined the French Thomson-CSF Radar System Division group in 1978 and moved to Alcatel-Space in 1983, where he worked on the space probe Giotto. He joined the Office National d'Etudes et de Recherches en Aéronautique, Toulouse, France, in 1984, and is specialized in microwave system design, mainly oriented to the prevention of natural risks. He obtained the MR grade (Maître de Recherches) at ONERA in 2001.



**Jean-Claude Poussière** was born in France in 1948.

He has been with the Office National d'Etudes et de Recherches en Aéronautique, Toulouse, France as a Technician for 35 years. His long experience in RF electronics has been fruitful for the design of mechanical parts and for the mounting of the system.



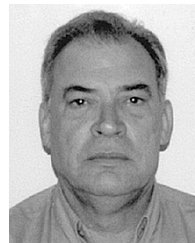
**Yann H. Kerr** (M'88–SM'01) received the engineering degree in radar and telecommunications from the Ecole Nationale Supérieure de l'Aéronautique et de l'Espace, Toulouse, France, the M.Sc. degree in electronics and electrical engineering from Glasgow University, Glasgow, U.K., and the Ph.D. degree in remote sensing and hydrology from the Université Paul Sabatier, Toulouse, France.

From 1980 to 1985, he was with the Centre National d'Etudes Spatiales, Toulouse, France. In 1985, he joined the Laboratoire d'Etudes et de Recherches en Télédétection Spatiale, Toulouse, France, as a Research Scientist. From May 1987 to December 1988, he was on leave of absence to work at the Jet Propulsion Laboratory, California Institute of Technology, Pasadena. He is currently with the Centre d'Etudes Spatiales de la Biosphère, Toulouse. His fields of interest are in the theory and techniques for microwave and thermal infrared remote sensing of the earth, with emphasis on hydrology and vegetation monitoring. He is currently the Lead Investigator of the ESA/CNES/CDTI Earth Explorer Opportunity Soil Moisture and Ocean Salinity missions, which is currently in phase C/D.



**Michel Déjus** received the Eng. degree in telecommunications from the Ecole Nationale Supérieure des Telecommunications de Bretagne, Bretagne, France, in 1992.

Since 1984, he has been with Centre National d'Etudes Spatiales (CNES), Toulouse, France, and since 1992, he has with the Antenna Department of the CNES Toulouse center. He is in charge of different types of activities in relation to antennas such as management of flight model development, management of investigation project, and management of software development.



**Roger Durbe** received the Diplôme de Technologie in physics from the Universitaire de Montpellier, Montpellier, France, in 1971.

He is currently a Research Engineer with Météo-France, Centre National de Recherches Meteorologiques (CNRM), Toulouse, France. He is Head of the electronics laboratory of Météo-France/CNRM. Since 1987, he was involved in many field experiments making use of ST VHF radars, enabling the retrieval of wind speed profiles into the troposphere. He has contributed to the

field campaigns FRONT 87, PYREX 90, MAP 99, ESCOMPTE 2001, and to the development of the RASS (Radio Acoustic Sound System), enabling the retrieval of air temperature profiles into the troposphere. His team at Météo-France/CNRM has put a lot of effort into the making of the fully automatic system of control, rotation, and acquisition of LEWIS, both from a technical and logistics point of view.



**Patricia de Rosnay** received the M.S. degree in oceanography, meteorology, and environmental sciences and the Ph.D. degree, both from the University Pierre et Marie Curie (Paris 6), France, in 1994 and 1999, respectively.

She is currently a Research Scientist with the Centre National de Recherches Spatiales, Centre d'Etudes Spatiales de la Biosphère, Toulouse, France. Her current research interests are focused on passive microwave remote sensing of soil moisture and the study of large-scale land surface processes.

She is involved in several land surface modeling activities such as GSWP2, PILPS, AMMA, and is now working on soil moisture remote sensing on field scale with the SMOSREX field experiment and complementary scale with the SMOS project.



**Jean-Christophe Calvet** received the engineering degree in agronomy from the Institut National Agronomique Paris-Grignon, Paris, France, and the engineering degree in meteorology from the Ecole Nationale de la Météorologie, Toulouse, France.

In 1990, he joined Météo-France, Centre National de Recherches Meteorologiques, Toulouse, France, and has been working in the field of remote sensing and land surface modeling, for applications in meteorology. His most recent works concern the analysis of soil moisture and the representation of an interactive

vegetation in climate models. He was involved with the scientific team of the Soil Moisture and Ocean Salinity (SMOS) project. He has contributed to the development of the SMOS land parameter retrieval algorithms, to field experiments to validate the SMOS products, and to the demonstration of the possibility to assimilate SMOS data into land surface models.